Journal of Power Sources 214 (2012) 344–350

Contents lists available at SciVerse ScienceDirect

Journal of Power Sources

journal homepage: www.elsevier.com/locate/jpowsour

Short communication

Enhanced electrochemical properties of $LiFe_{1-x}Mn_xPO_4$/C composites synthesized from $FePO_4 \cdot 2H_2O$ nanocrystallites

Li Chen, Yong-Qiang Yuan, Xia Feng, Ming-Wei Li*

Department of Chemistry, Tianjin University, Tianjin 300072, People's Republic of China

HIGHLIGHTS

- Pre-synthesized $FePO_4 \cdot 2H_2O$ nanocrystallites are used to synthesize $LiFe_{1-x}Mn_xPO_4$.
- Well-ordered $LiFe_{1-x}Mn_xPO_4$ ($x = 0.85, 0.75, 0.65$) nanostructures form.
- $LiFe_{1-x}Mn_xPO_4$/C composites have enhanced electrochemical properties.
- $LiFe_{0.25}Mn_{0.75}PO_4$ sample exhibits the best electrochemical performances.

ARTICLE INFO

Article history:
Received 12 January 2012
Received in revised form
23 April 2012
Accepted 27 April 2012
Available online 4 May 2012

Keywords:
Lithium-ion battery
Cathode material
Lithium manganese phosphate
Iron substitution

ABSTRACT

The high discharge potential of $LiMnPO_4$, 4.1 V vs. Li/Li^+, and its theoretical capacity of 170 mAh g^{-1} make it a promising candidate as a cathode material in lithium-ion batteries. But extremely low electronics conductivity, slow lithium diffusion kinetics, and the Jahn-Teller effect of Mn^{3+} limit the electrochemical performances of $LiMnPO_4$. In this work, the pre-synthesized and defined $FePO_4 \cdot 2H_2O$ nanocrystallites are used as one of the raw materials to synthesize $LiFe_{1-x}Mn_xPO_4$/C ($x = 0.85, 0.75, 0.65$) composites via solid-state reactions. The synthesized $LiFe_{1-x}Mn_xPO_4$ samples show well-crystallized structures and have enhanced electrochemical properties. There exist two plateaus around 3.5 and 4.1 V on both of their charge and discharge curves. Among the samples, the $Fe_{0.25}Mn_{0.75}PO_4$ one exhibits the longest high-voltage charge/discharge plateau at 4.10 V/4.05 V, and has an average discharge voltage of ~3.78 V vs. Li/Li^+ and a discharge capacity of ~130 mAh g^{-1} at 0.05 C rate. For the $Fe_{0.25}Mn_{0.75}PO_4$ sample, the noticeable improvement of its electrochemical performances is mainly attributed to iron substitution, the appropriate Mn/Fe ratio, and the well-ordered crystal structure forming by using $FePO_4 \cdot 2H_2O$ nanocrystallites as one of the raw materials.

1. Introduction

Olivine structural lithium transition-metal phosphates $LiMPO_4$ (M = Fe, Mn, Co, and Ni) were found to be ones of the most promising candidates as the cathode materials for large-scale lithium-ion batteries due to their large theoretical capacities and excellent thermal stability [1–4]. Among them, $LiFePO_4$ has the inherent characteristics of low-cost and environmental friendliness, so it has been extensively studied and its electrochemical properties have been greatly improved by cation substitution/doping and surface modification with conductive materials coating to enhance its low conductivity [5–11].

$LiMnPO_4$ is of particular interest to battery industry because of its higher theoretical energy density than $LiFePO_4$. It has higher discharge potential (4.1 V vs. Li/Li^+) than $LiFePO_4$ (3.4 V vs. Li/Li^+), and its theoretical capacity of 170 mAh g^{-1} is almost the same as $LiFePO_4$. However, the even lower electronic conductivity and slow lithium diffusion limit $LiMnPO_4$ electrochemical performances [2,3]. Another unavoidable problem is the electrochemical stability of $LiMnPO_4$ is badly affected by the Jahn-Teller effect of Mn^{3+}. During cycling, the shrinkage of about 8.9% occurs during $LiMnPO_4$ delithiated to form $MnPO_4$, but only 6.8% during $LiFePO_4$ delithiated to form $FePO_4$. Additionally, the cell volume of $LiFe_{1-x}Mn_xPO_4$ increases with increasing Mn^{2+} content x, while the volume is almost constant in $Fe_{1-x}Mn_xPO_4$ at different Mn^{3+} content x [12–15]. Therefore, appropriate iron substitution is beneficial to keeping stable volume of $LiFe_{1-x}Mn_xPO_4$ during the lithium extraction/insertion.

* Corresponding author. Tel.: +86 22 27890272; fax: +86 22 27403475.
E-mail address: mingweili@tju.edu.cn (M.-W. Li).

0378-7753/$ – see front matter © 2012 Elsevier B.V. All rights reserved.
doi:10.1016/j.jpowsour.2012.04.089

Inspired by the success of $LiFePO_4$, researchers have tried similar methods to improve the electrochemical properties of $LiMnPO_4$ [16–21]. It has been reported that an improvement in kinetics was realized as partial Mn ions were substituted by Fe to form $LiFe_{1-x}Mn_xPO_4$, such as $LiFe_{0.2}Mn_{0.8}PO_4$ [13,20]. The Fe substitution in Mn-sites probably has two main benefits: one is enhancing the transport properties of materials; the other is decreasing the Jahn–Teller effect of Mn^{3+}.

Some researchers synthesized monoclinic phase $FePO_4 \cdot 2H_2O$ nanoparticles at first, and then lithiated them to form $LiFePO_4$/C composites, which show improved high-rate charge/discharge capability and long-term cyclability [21,22]. Wang et al. synthesized $LiFePO_4$/C composite using a core–shell structural precursor $FePO_4$/polyaniline, and suggested that the $LiFePO_4$/C nanoparticles form by an *in situ* polymerization restriction mechanism [23]. Additionally, $LiMnPO_4$ has ever been synthesized from a $MnPO_4 \cdot 2H_2O$ precursor. It was reported that the $MnPO_4 \cdot 2H_2O$ nanoparticles facilely react with lithium source and form $LiMnPO_4$ via solid-state reactions at 550 °C [24,25], and the synthesized $LiMnPO_4$ shows improved electrochemical properties.

In this work, iron substitution is utilized to improve the electrochemical properties of $LiMnPO_4$. To synthesize a well-ordered $LiFe_{1-x}Mn_xPO_4$ crystal structure, the $FePO_4 \cdot 2H_2O$ nanocrystallites are pre-synthesized and defined, and then are used as one of the raw materials to form a precursor by ball milling with Li-, Mn-, PO_4-, and carbon-containing chemicals. The precursors finally form $LiFe_{1-x}Mn_xPO_4$/C (x = 0.85, 0.75, 0.65) composites via solid-state reactions at 550 °C. The synthesized $LiFe_{1-x}Mn_xPO_4$ nanoparticles exhibit well-ordered crystal structures, and show obvious enhanced electrochemical properties.

2. Experimental

$FePO_4 \cdot 2H_2O$ were pre-synthesized by a spontaneous precipitation method. Equimolar aqueous solution of H_3PO_4 and $FeCl_2$ with a concentration of 0.1 M was added into a continuous stirred beaker in water bath at 60 °C. After 10 min, excess H_2O_2 solution (30 wt.%), the molar ratio of $H_2O_2/FeCl_2$ = 1.1/2, was fed into the beaker. The pH value of the mixed solution was controlled between 4.0 and 5.0 by adding ammonia. At the initial stage of the reaction, there appeared precipitate in the beaker. After stirring 15 min, the precipitate was filtered and washed with de-ionized water until its pH value became neutral. The obtained precipitate was dried at 120 °C for 12 h.

$LiFe_{1-x}Mn_xPO_4$/C (x = 0.85, 0.75, 0.65) composites were synthesized by solid-state reactions after a two-stage ball milling process. Stoichiometric amounts of the above synthesized $FePO_4 \cdot 2H_2O$, Li_2CO_3, $Mn(CH_3COO)_2 \cdot 4H_2O$, $NH_4H_2PO_4$, and sucrose (25 wt.% of $LiFe_{1-x}Mn_xPO_4$) were dissolved in de-ionized water. This solution was wet ball-milled for 10 h at room temperature and dried in a vacuum oven at 80 °C for 12 h. The dried precursor was heated at 300 °C for 5 h under argon atmosphere for its main decomposition. Then the decomposed precursor was ball-milled for 10 h at room temperature. Finally the precursor was calcined at 550 °C for 10 h in an Ar atmosphere until the expected $LiFe_{1-x}Mn_xPO_4$/C composites formed. As a contrast, $LiMnPO_4$/C (i.e., x = 1.0) composite was also synthesized using the same synthesis condition only without $FePO_4 \cdot 2H_2O$ in the precursor.

To study the thermal stability of the precursor and optimize the synthesis condition, thermogravimetric and differential scanning calorimetry (TG-DSC) analyses were performed using a simultaneous thermal analyzer (STA 409 PC/PG, NETZSCH). About 10 mg sample was heated from room temperature to appropriate temperatures in N_2 at a heating rate of 10 °C min^{-1}.

The crystalline structures of the samples were analyzed by a powder X-ray diffractometer (XRD, D/max 2500 V/PC, Rigaku) using Cu Kα radiation. Lattice parameters were calculated from the refined XRD patterns. The crystallite size was obtained from XRD results and calculated by Scherrer formula, $d = k \cdot \lambda/(\beta \cdot \cos\theta)$, where d (nm) is the mean crystallite size, k (= 0.89) is the shape factor of particles, λ (= 0.154056 nm) is the X-ray wavelength, β (radian) is the half-width of the main diffraction peak, and θ (radian) is the Bragg angle of main diffraction peak. Morphology and microstructure of the samples were investigated using a scanning electron microscope (SEM, XL30, Philips) and a field-emission high-resolution transmission electron microscope (HRTEM, Tecnai G^2 F20, FEI) with an energy-dispersive X-ray spectroscopy (EDX). An infrared carbon and sulfur analyzer (CS-901B, Haotianhui) was used to analyze the carbon content of the samples.

The electrochemical measurements were performed using 2032 coin-type cells with lithium metal as the anode. For cathode fabrication, at first a mixture was made by well mixing the synthesized $LiFe_{1-x}Mn_xPO_4$/C composite, conductive carbon black (Super P), and N-methyl-2-pyrrolidinone (NMP) in a weight ratio of 80/10/10. Then the mixture was spread onto aluminum foil and formed a uniform thin layer with a thickness of 150 μm. It was dried at 80 °C in a vacuum oven for 12 h to remove NMP. The coated aluminum foil was dried at 120 °C overnight under vacuum and punched into 13 mm diameter disks, which served as the cathode. 1 M $LiPF_6$ in ethylene carbonate and dimethyl carbonate (50/50 in volume) was used as the electrolyte. All cells were assembled in an Ar-filled glove box. The coin cells were placed on a battery testing system (CT2001A, LAND) with current density at 0.05 C (1 C = 170 mA g^{-1}) in a voltage window between 2.5 and 4.5 V vs. Li/Li^+ at room temperature.

3. Results and discussion

At first, $FePO_4 \cdot 2H_2O$ nanocrystallites were synthesized according to the reaction

$$2FeCl_2 + 2NH_4H_2PO_4 + H_2O_2 = 2FePO_4 \cdot 2H_2O + 2NH_4Cl + 2HCl$$

The precipitation was washed, dried, and used as one of the raw materials to synthesize $LiFe_{1-x}Mn_xPO_4$/C composites.

Fig. 1 shows the XRD pattern of the dried precipitation. The pattern matches well with the monoclinic iron phosphate hydrate,

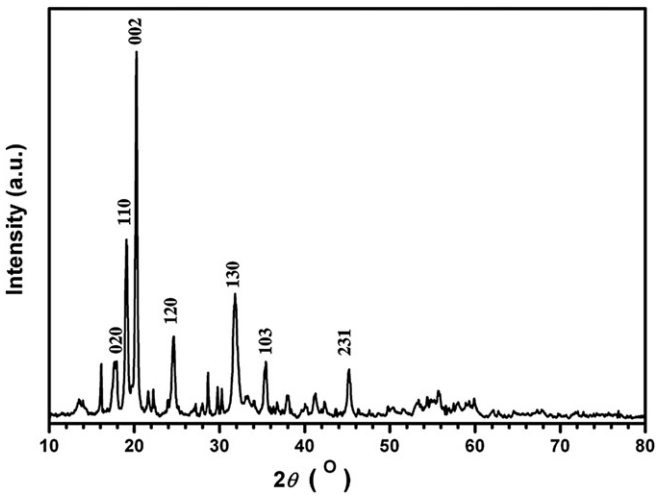

Fig. 1. XRD pattern of the synthesized $FePO_4 \cdot 2H_2O$ sample.

i.e., $FePO_4 \cdot 2H_2O$ (JCPDS 76-0451). The sample's lattice parameters are listed in Table 1. Its cell volume is larger than the values of later synthesized $LiFe_{1-x}Mn_xPO_4$ samples. Its mean crystalline size is about 54 nm. The $FePO_4 \cdot 2H_2O$ nanocrystallites should shrink as losing their crystallization water during heat treatment.

Fig. 2 exhibits the TG-DSC curves of the dried $FePO_4 \cdot 2H_2O$ sample. There occurred a rapid weight loss (~19.4 wt.%) mostly between 150 and 190 °C. The lost weight is close to the percentage (19.3 wt.%) of crystallization water in $FePO_4 \cdot 2H_2O$. The sample's weight hardly changed after 200 °C. The DSC curve shows that there is only an endothermic peak at 188 °C. It indicates that the $FePO_4 \cdot 2H_2O$ sample lost all its crystallization water in one step. These results coincide with previous literature [22].

Fig. 3 is the SEM image of the as-synthesized $FePO_4 \cdot 2H_2O$ sample. The sample consists of many nano-sized granules, whose size matches with the XRD result, i.e., ~54 nm. It implies that the $FePO_4 \cdot 2H_2O$ granules are well-crystallized. Experimentally, the $FePO_4 \cdot 2H_2O$ nanocrystallites were ball-milled with Li-, Mn-, PO_4-, and carbon-containing materials, i.e., Li_2CO_3, $Mn(CH_3COO)_2 \cdot 4H_2O$, $NH_4H_2PO_4$, and sucrose, to form a precursor. During heat treatment, the precursor lost its crystallization water, decomposed, and finally formed $LiFe_{1-x}Mn_xPO_4/C$ ($x = 0.85, 0.75, 0.65$) composites via solid-state reactions.

In this study, sucrose played multi-functions that should be discussed later. According to literature [26,27], the thermal decomposition of pure sucrose starts at about 186 °C in N_2 atmosphere, and the most weight loss occurs between 220 and 400 °C. Complete carbonization of sucrose needs a temperature beyond 700 °C. It was reported that $Mn(CH_3COO)_2 \cdot 4H_2O$ loses all crystallization water under heat treatment at about 120 °C, and $Mn(CH_3COO)_2$ thermally decomposes to MnO around 320 °C [28]. Although in air pure $LiCO_3$ has a high decomposition temperature (~1310 °C), Li_2CO_3 can react with $NH_4H_2PO_4$, and releases CO_2 and NH_3 between 180 and 400 °C [27].

Fig. 4 shows the TG-DSC curves of the dried precursor for synthesizing $LiFe_{0.25}Mn_{0.75}PO_4$ after wet ball milling. The TG curve exhibits three main stages of weight loss. From 100 to 170 °C, the precursor loses about 8.0% weight, which is mainly attributed to the loss of crystallization water in $Mn(CH_3COO)_2 \cdot 4H_2O$. From 170 to 250 °C, the precursor rapidly loses about 20.0% weight, which is mainly ascribed to the thermal decomposition of $FePO_4 \cdot 2H_2O$, $Mn(CH_3COO)_2$, and sucrose. There is an obvious endothermic DSC peak at around 189 °C, which coincides with the endothermic peak in Fig. 2. At this stage, $NH_4H_2PO_4$ also starts to react with $LiCO_3$ and releases NH_3 and CO_2. A continuous weight loss (~6.0%) between 250 and 500 °C is related to the continuous thermal decomposition of sucrose, $LiCO_3$, and $NH_4H_2PO_4$.

There is an exothermic DSC peaks at 520 °C, but no evident weight loss is found on the TG curve above 500 °C. It implies that a solid–state reaction or phase transfer probably occurred at the temperature.

According to the TG-DSC results, the synthesis condition was chosen and optimized in the experiments. The precursor is heated at 300 °C for 5 h for its main weight loss. Then the decomposed precursor is ball-milled to form small granules. To synthesize the finial $LiFe_{1-x}Mn_xPO_4/C$ nanoparticles, the precursor is heated at a lower temperature (550 °C) for 10 h.

Table 1
Lattice parameters and mean crystalline sizes (d) of the samples.

Sample	a (Å)	b (Å)	c (Å)	Volume (Å^3)	d (nm)
$FePO_4 \cdot 2H_2O$	5.3105	9.7658	8.7413	453.29	54
$LiMnPO_4$	6.0998	10.4403	4.7429	302.05	41
$LiFe_{0.15}Mn_{0.85}PO_4$	6.0850	10.4398	4.7465	301.53	30
$LiFe_{0.25}Mn_{0.75}PO_4$	6.0846	10.4289	4.7358	300.51	41
$LiFe_{0.35}Mn_{0.65}PO_4$	6.0741	10.4160	4.7305	299.29	51

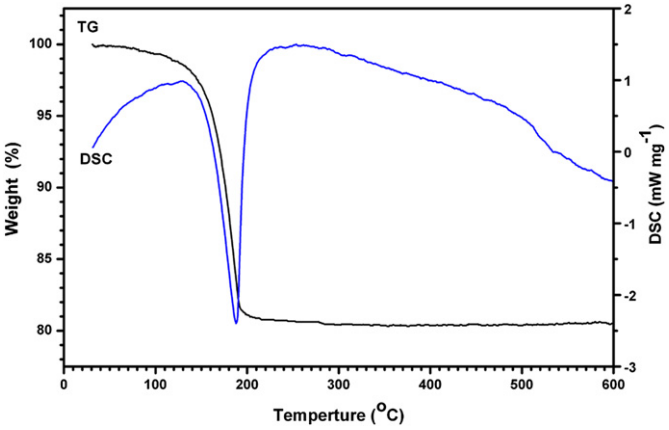

Fig. 2. TG-DSC curves of the synthesized $FePO_4 \cdot 2H_2O$ sample.

Fig. 5 shows the XRD patterns of synthesized $LiMnPO_4/C$ and $LiFe_{1-x}Mn_xPO_4/C$ samples. The diffraction peaks indicate that there is crystalline phase formed in each sample. The crystal structure is an olivine structure indexed to orthorhombic Pmnb similar to $LiMnPO_4$ (JCPDS 74-0375) or $LiFePO_4$ (JCPDS 83-2092). Neither Li_2CO_3 nor Li_2O is detected in the XRD results. Their main diffraction peaks should be at 31.80 ° (JCPDS 87-0729) and 33.58 ° (JCPDS 77-2144) respectively. According to the JCPDS cards, the main diffraction peaks of $LiMnPO_4$ and $LiFePO_4$ are at 35.14 and 35.59 ° respectively. The synthesized samples' main peaks locate at 35.19, 35.17, 35.21, and 35.27 °, which increase with their increasing Fe contents. The lattice parameters and mean crystalline sizes are listed in Table 1. The samples have near lattice parameters, and the cell volumes of Fe-substituted samples are smaller than that of $LiMnPO_4$. The XRD results indicate that the samples consist of well-crystallized $LiFe_{1-x}Mn_xPO_4$ nanoparticles.

Fig. 6 presents the SEM images of the as-synthesized $LiFe_{1-x}Mn_xPO_4/C$ composites. The particles tightly or loosely aggregate each other with an average particle size of 100–200 nm. It is noticeable that the samples' morphologies closely relate with their carbon contents. From Fig. 6(a) to (d), the samples' carbon contents decrease from 9.6 to 6.3 wt.%. As can be seen in Fig. 6, the higher carbon content a sample has, the more compacted particles the sample shows. The $LiMnPO_4/C$ sample has the highest carbon

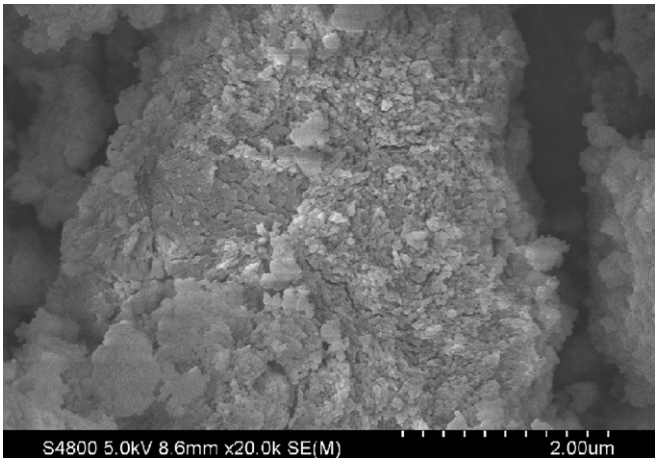

Fig. 3. SEM image of the as-synthesized $FePO_4 \cdot 2H_2O$ sample.

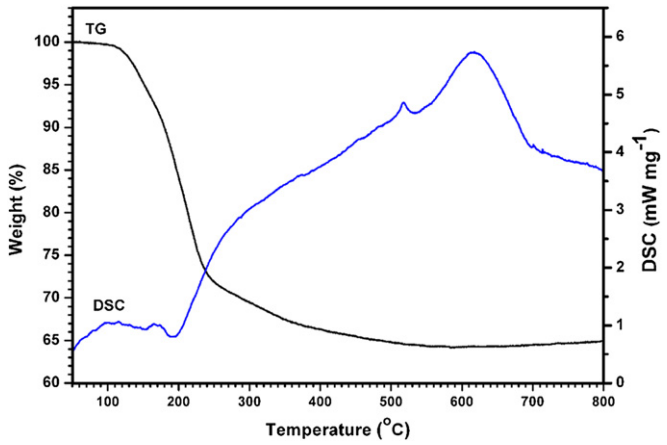

Fig. 4. TG-DSC curves of the dried precursor after $FePO_4 \cdot 2H_2O$ being wet ball-milled with other raw materials and dried in a vacuum oven at 80 °C for 12 h.

content (9.6%), so its particles tightly bond. The $LiFe_{0.15}Mn_{0.85}PO_4/C$ sample with a carbon content of 8.4% has apparent space among its bonded particles. However, the particles in $LiFe_{0.25}Mn_{0.75}PO_4/C$ and $LiFe_{0.35}Mn_{0.65}PO_4/C$ samples loosely disperse due to their lower carbon contents, which are 7.4 and 6.3% respectively.

The different carbon contents mainly originate from the different quantity of $Mn(CH_3COO)_2 \cdot 4H_2O$. The more $Mn(CH_3COO)_2 \cdot 4H_2O$ is used in the precursor, the higher carbon content is found in the sample.

In this study, the main function of sucrose is to reduce Fe^{3+} to Fe^{2+} under heat treatment. Excess sucrose and $Mn(CH_3COO)_2 \cdot 4H_2O$ forms carbon coating on the $LiFe_{1-x}Mn_xPO_4$ nanoparticles. It was reported that carbon coating can limit the crystal growth of $LiFePO_4$ by an *in situ* polymerization restriction mechanism [23]. Carbon also bonds particles together and enhances the transport properties of materials, thus improving the electrochemical performances of cathode materials. However, as the precursor was heated at only 550 °C, the sucrose probably was not completely carbonized, and the formed CH_x with a lower conductivity. Additionally, carbon also decreases electrodes tap density and increases the battery volume.

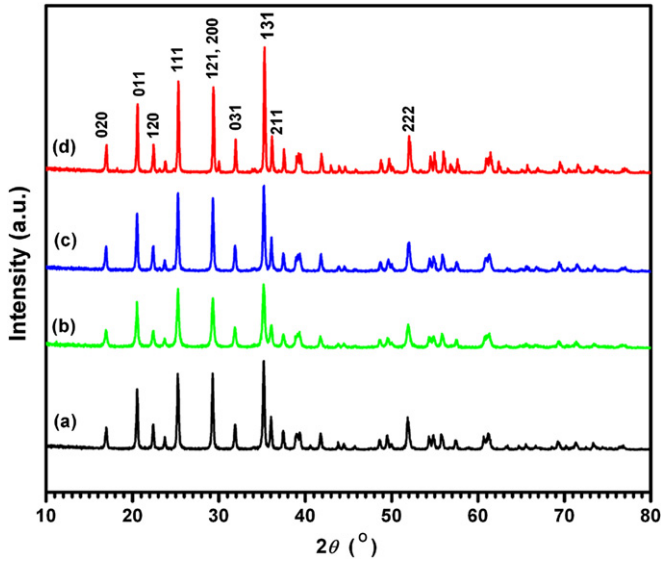

Fig. 5. XRD patterns for (a) $LiMnPO_4/C$, (b) $LiFe_{0.15}Mn_{0.85}PO_4/C$, (c) $LiFe_{0.25}Mn_{0.75}PO_4/C$, and (d) $LiFe_{0.35}Mn_{0.65}PO_4/C$ composites.

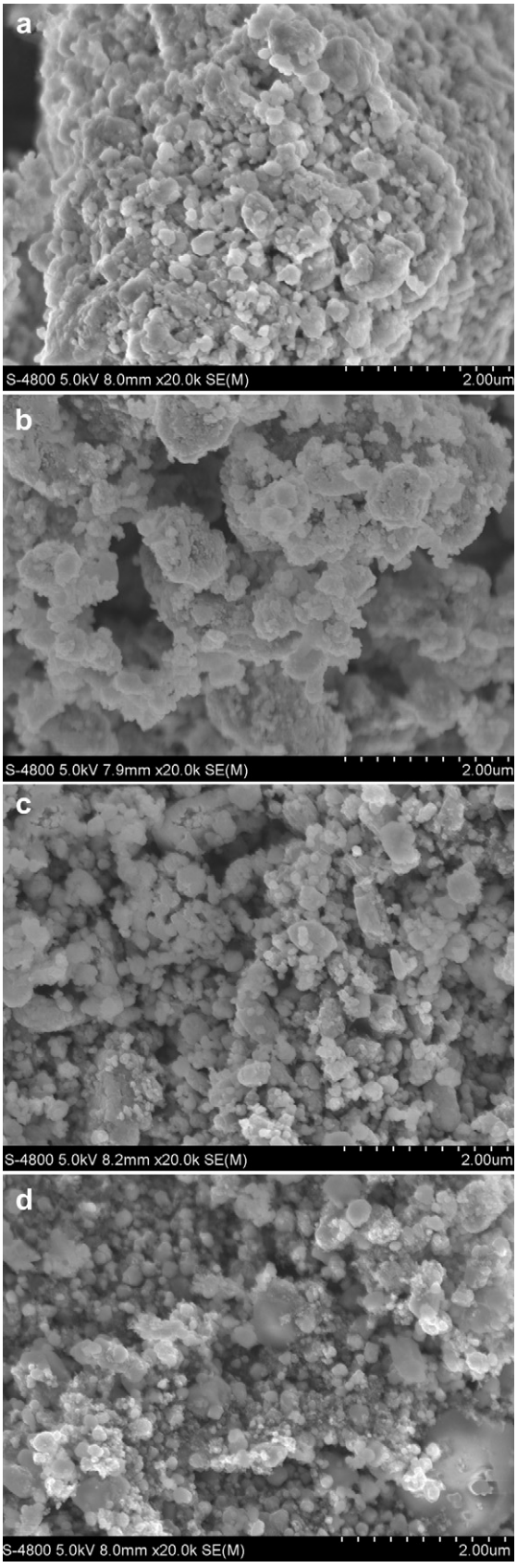

Fig. 6. SEM images for (a) $LiMnPO_4/C$, (b) $LiFe_{0.15}Mn_{0.85}PO_4/C$, (c) $LiFe_{0.25}Mn_{0.75}PO_4/C$, and (d) $LiFe_{0.35}Mn_{0.65}PO_4/C$ composites.

Therefore, the quantity of sucrose needs optimizing. However, carbon contents in the four samples are near and change from 9.6 to 6.3%. The $LiFe_{0.25}Mn_{0.75}PO_4$/C sample exhibits the best electrochemical properties and its carbon content is 7.6%.

As listed in Table 1, the mean crystalline sizes of $LiFe_{1-x}Mn_xPO_4$ ($x = 0.85, 0.75, 0.65$) decrease with increasing carbon contents and decreasing Mn contents. But the $LiMnPO_4$/C sample, with the highest carbon content and Mn content, has the biggest mean crystalline size. It suggests that the iron substitution promotes the formation of smaller $LiFe_{1-x}Mn_xPO_4$ nanocrystallites.

To get a better overview at a nanostructural scale, HRTEM and EDX were used to analyze the samples. It is observed that the samples are mainly composed of spherical particles of about 40–100 nm being coated by amorphous carbon. Fig. 7(a) shows a selected bigger particle of $LiFe_{0.25}Mn_{0.75}PO_4$ sample. The particle is covered by a 2-nm thickness carbon layer, and almost has the same Fe content (Fe/Mn = 19/81) at its center and brim. The crystallite exhibits a well-defined orthorhombic symmetry, and its atomic layers are clear. There are different lattice space of 0.43, 0.30, and 0.25 nm, corresponding to (0 1 1), (2 0 0), and (1 3 1) atomic layers. It indicates that the particle has a well-ordered and well Fe-substituted crystal structure.

To investigate the formation mechanism of $LiFe_{1-x}Mn_xPO_4$, EDX was used to analyze the element atomic percents of a selected particle of $LiFe_{0.35}Mn_{0.65}PO_4$ sample. Fig. 7(b) shows the Fe content at the particle's brim is higher than that at its center. It means that Fe is somehow rich at the particle' brim as Fe content increasing.

Fig. 8 exhibits the samples' specific discharge capacities at 0.05 C rate. $LiMnPO_4$/C has a lowest specific capacity at about 22 mAh g^{-1}. After iron substitution, the $LiFe_{1-x}Mn_xPO_4$/C samples exhibit great improved electrochemical properties. $LiFe_{0.15}Mn_{0.85}PO_4$/C has a specific capacity of 77 mAh g^{-1} after the 8th cycle. Noticeably, $LiFe_{0.25}Mn_{0.75}PO_4$/C shows a stable specific capacity at about 130 mAh g^{-1} from the second cycle. Although the specific capacity of $LiFe_{0.35}Mn_{0.65}PO_4$/C is bigger than 130 mAh g^{-1} at the first cycle, it rapidly falls to about 117 mAh g^{-1} after the 8th cycle.

More details of the samples' performances can be seen in Figs. 9 and 10. Fig. 9 shows the samples' charge/discharge curves at the 3rd cycles when the cells were charged/discharged at 0.05 C rate in a voltage window between 2.5 and 4.5 V $LiMnPO_4$/C sample has a worse specific capacity of 24 mAh g^{-1} and its average discharge voltage is 3.67 V. For $LiFe_{0.15}Mn_{0.85}PO_4$/C, the two values are 67 mAh g^{-1} and 3.78 V respectively. While $LiFe_{0.25}Mn_{0.75}PO_4$/C has both the biggest specific capacity (~130 mAh g^{-1}) and the highest discharge voltage (~3.78 V). However, with Fe content increasing, the $LiFe_{0.35}Mn_{0.65}PO_4$/C sample's specific capacity and discharge voltage fall to 127 mAh g^{-1} and 3.64 V respectively. An appropriate Fe/Mn ratio is important to the $LiFe_{1-x}Mn_xPO_4$ samples' properties.

Generally, during the 1st cycle there occurs irreversible capacity loss, which is partly caused by the formation of solid electrolyte interface (SEI) film [29]. Fig. 10 shows the different behavior of $LiMnPO_4$ and $LiFe_{0.25}Mn_{0.75}PO_4$ during their first four cycles, reflecting such capacity loss. Despite its unstable charge capacity at the first two cycles, $LiFe_{0.25}Mn_{0.75}PO_4$ exhibits stable discharge capacities around 130 mAh g^{-1}. Its discharge capacity became stable from the 3rd cycle. As a contrast, the $LiMnPO_4$ sample shows worse capacity and stability.

Each $LiFe_{1-x}Mn_xPO_4$ sample shows two charge plateaus near 3.55 and 4.12 V, and also has two distinct discharge plateaus near 4.05 and 3.50 V. But the $LiMnPO_4$ sample only has an indistinct discharge plateau near 3.95 V, and hardly shows a charge voltage plateau. This phenomenon had been found as soon as $LiFe_{1-x}Mn_xPO_4$ was researched as cathode materials [1,12–14]. Undoubtedly, these charge/discharge voltage plateaus are related with the redox couples Mn^{3+}/Mn^{2+} and Fe^{3+}/Fe^{2+}, whose potential respectively is 4.1 and 3.5 V vs. Li/Li^+.

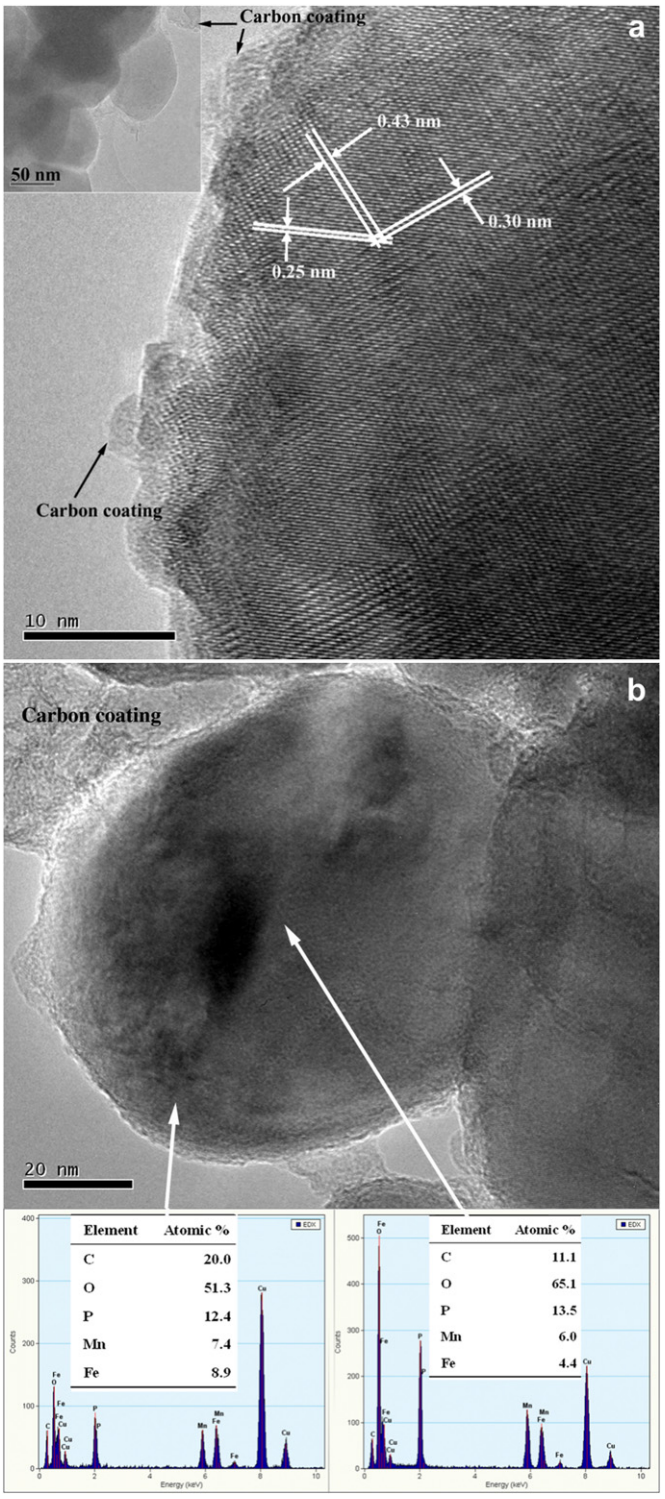

Fig. 7. HRTEM images for (a) a selected $LiFe_{0.25}Mn_{0.75}PO_4$ particle (the inset is several spherical particles bonded by carbon), and (b) $LiFe_{0.35}Mn_{0.65}PO_4$ particles. The EDX spectra are detected at the brim and the center of a selected particle.

$LiMnPO_4$ has higher discharge potential of 4.1 V vs. Li/Li^+ and bigger theoretical capacity of 170 mAh g^{-1}, but the worse transport properties badly affect its electrochemical performances. In this study, the synthesized $LiMnPO_4$ sample hardly shows charge/

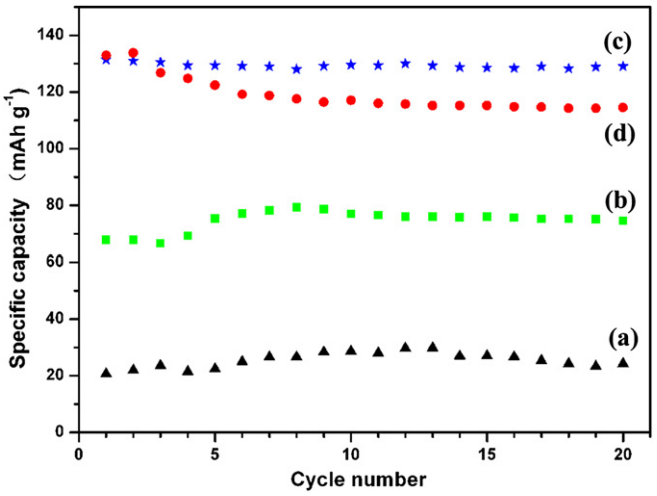

Fig. 8. Discharge specific capacities at 0.05 C rate for (a) $LiMnPO_4$/C, (b) $LiFe_{0.15}Mn_{0.85}PO_4$/C, (c) $LiFe_{0.25}Mn_{0.75}PO_4$/C, and (d) $LiFe_{0.35}Mn_{0.65}PO_4$/C composites.

discharge plateaus, as shown in Fig. 10(a). After iron substitution, all the $LiFe_{1-x}Mn_xPO_4$/C composites exhibit great improvement in their electrochemical performances. Theoretically, the length ratio of the high-voltage plateau and the low-voltage plateau should be equal to the Mn/Fe ratio in $LiFe_{1-x}Mn_xPO_4$ material due to their almost same theoretical capacities. Interestingly, the $LiFe_{0.25}Mn_{0.75}PO_4$ sample has the longest high-voltage charge/discharge plateau at 4.10 V/4.05 V despite its Mn/Fe ratio being less than the $LiFe_{0.35}Mn_{0.65}PO_4$ sample. As a result, $LiFe_{0.25}Mn_{0.75}PO_4$/C sample also exhibits the best electrochemical properties.

The improvement of $LiFe_{1-x}Mn_xPO_4$/C composites' performance possibly involves of several reasons, including Fe substitution in Mn-sites, appropriate Mn/Fe ratio, crystallite size, crystal structure, and appropriate carbon content. We consider that the appropriate Mn/Fe ratio in the $LiFe_{0.25}Mn_{0.75}PO_4$ sample plays a key role for its best performances. Another important reason is the usage of pre-synthesized $FePO_4 \cdot 2H_2O$ nanoparticles as one of the raw materials to synthesize well-ordered $LiFe_{0.25}Mn_{0.75}PO_4$ nanocrystallites. The well-ordered crystal structure might enhance the transport properties of $LiFe_{0.25}Mn_{0.75}PO_4$, thus improve its electrochemical properties.

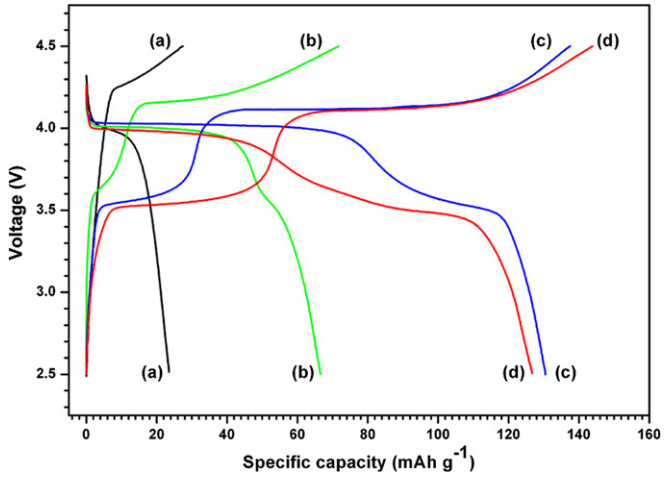

Fig. 9. Charge/discharge curves of their 3rd cycles at 0.05 C rate for (a) $LiMnPO_4$/C, (b) $LiFe_{0.15}Mn_{0.85}PO_4$/C, (c) $LiFe_{0.25}Mn_{0.75}PO_4$/C, and (d) $LiFe_{0.35}Mn_{0.65}PO_4$/C composites.

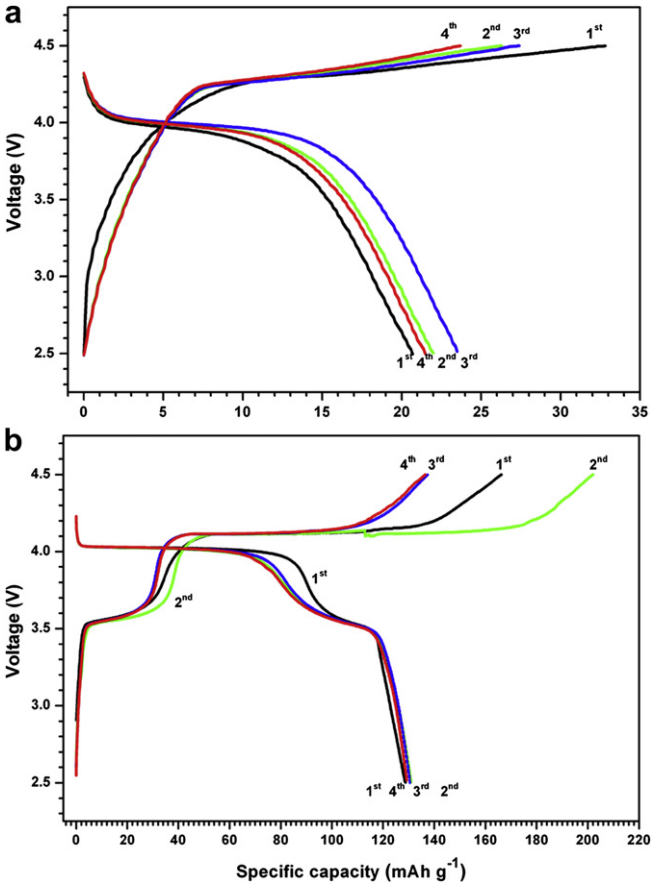

Fig. 10. Charge/discharge curves of their first four cycles at 0.05 C rate for (a) $LiMnPO_4$/C and (b) $LiFe_{0.25}Mn_{0.75}PO_4$/C composites.

4. Conclusion

In this work, to improve the electrochemical performances of $LiMnPO_4$, pre-synthesized $FePO_4 \cdot 2H_2O$ nanocrystallites are used as one of the raw materials to synthesize $LiFe_{1-x}Mn_xPO_4$/C ($x = 0.85$, 0.75, 0.65) composites via solid-state reactions. The synthesized $LiFe_{1-x}Mn_xPO_4$ nanocrystallites show well-ordered and Fe-doped crystal structures. Their specific capabilities and average discharge voltages have been noticeably improved compare with the synthesized $LiMnPO_4$ sample. There exist two plateaus around 3.5 and 4.1 V on their charge/discharge curves. The $LiFe_{0.25}Mn_{0.75}PO_4$/C sample exhibits the longest high-voltage charge/discharge plateau at 4.10 V/4.05 V, which results in its best electrochemical properties. We consider that such improvement of $LiFe_{1-x}Mn_xPO_4$ samples' performances is mainly attributed to the appropriate iron substitution, and well-ordered crystal structure forming by using the well-crystallized $FePO_4 \cdot 2H_2O$ nanoparticles as one of the raw materials.

References

[1] A.K. Padhi, K.S. Nanjundaswamy, J.B. Goodenough, J. Electrochem. Soc. 144 (1997) 1188–1194.
[2] M.S. Whittingham, Chem. Rev. 104 (2004) 4271–4301.
[3] Y.-N. Xu, W.Y. Ching, Y.-M. Chiang, J. Appl. Phys. 95 (2004) 6583–6585.
[4] C.A.J. Fisher, V.M.H. Prieto, M.S. Islam, Chem. Mater. 20 (2008) 5907–5915.
[5] S.-Y. Chung, J.T. Bloking, Y.-M. Chiang, Nat. Mater. 1 (2002) 123–128.
[6] H. Xie, Z. Zhou, Electrochim. Acta 51 (2006) 2063–2067.
[7] R. Yang, X. Song, M. Zhao, F. Wang, J. Alloys Compd. 468 (2009) 365–369.
[8] C. Delacourt, C. Wurm, L. Laffont, J.-B. Leriche, C. Masquelier, Solid State Ionics 177 (2006) 333–341.

[9] T.-H. Teng, M.-R. Yang, S.-H. Wu, Y.-P. Chiang, Solid State Commun. 142 (2007) 389–392.
[10] Y. Wang, Y. Yang, X. Hu, Y. Yang, H. Shao, J. Alloys Compd. 481 (2009) 590–594.
[11] Y. Ge, X. Yan, J. Liu, X. Zhang, J. Wang, X. He, R. Wang, H. Xie, Electrochim. Acta 55 (2010) 5886–5890.
[12] A. Yamada, Y. Kudo, K.-Y. Liu, J. Electrochem. Soc. 148 (2001) A747–A754.
[13] A. Yamada, S.-C. Chung, J. Electrochem. Soc. 148 (2001) A960–A967.
[14] A. Yamada, M. Hosoya, S.-C. Chung, Y. Kudo, K. Hinokuma, K.-Y. Liu, Y. Nishi, J. Power Sources 119–121 (2003) 232–238.
[15] C. Delacourt, P. Poizot, M. Morcrette, J.-M. Tarascon, C. Masquelier, Chem. Mater. 16 (2004) 93–99.
[16] C. Hu, H. Yi, H. Fang, B. Yang, Y. Yao, W. Ma, Y. Dai, Electrochem. Commun. 12 (2010) 1784–1787.
[17] T. Shiratsuchi, S. Okada, T. Doi, J.-I. Yamaki, Electrochim. Acta 54 (2009) 3145–3151.
[18] B. Kang, G. Ceder, J. Electrochem. Soc. 157 (2010) A808–A811.
[19] X.-Z. Liao, Z.-F. Ma, Y.-S. He, X.-M. Zhang, L. Wang, Y. Jiang, J. Electrochem. Soc. 152 (2005) A1969–A1973.
[20] J. Hong, F. Wang, X. Wang, J. Graetz, J. Power Sources 196 (2011) 3659–3663.
[21] Y. Wang, J. Wang, J. Yang, Y. Nuli, Adv. Funct. Mater. 16 (2006) 2135–2140.
[22] M. Wang, Y. Xue, K. Zhang, Y. Zhang, Electrochim. Acta 56 (2011) 4294–4298.
[23] Y. Wang, Y. Wang, E. Hosono, K. Wang, H. Zhou, Angew. Chem. Int. Ed. 47 (2008) 7461–7465.
[24] J. Xiao, W. Xu, D. Choi, J.-G. Zhang, J. Electrochem. Soc. 157 (2010) A142–A147.
[25] L. Wang, W. Sun, X. He, J. Li, C. Jiang, Int. J. Electrochem. Sci. 6 (2011) 2022–2030.
[26] G.N. Richards, F. Shafizadeh, Aust. J. Chem. 31 (1978) 1825–1832.
[27] E.-H.M. Diefallah, Thermochim. Acta 202 (1992) 1–16.
[28] K. Wang, R. Cai, T. Yuan, X. Yu, R. Ran, Z. Shao, Electrochim. Acta 54 (2009) 2861–2868.
[29] S. Zhang, M.S. Ding, K. Xu, J. Allen, T.R. Jow, Electrochem. Solid-State Lett. 4 (2001) A206–A208.